Geochemistry Geophysics Geosystems G3
AN ELECTRONIC JOURNAL OF THE EARTH SCIENCES
Published by AGU and the Geochemical Society

Article
Volume 10, Number 9
25 September 2009
Q09006, doi:10.1029/2009GC002633
ISSN: 1525-2027

Advancing techniques to constrain the geometry of the seismic rupture plane on subduction interfaces a priori: Higher-order functional fits

Gavin P. Hayes and David J. Wald

National Earthquake Information Center, U.S. Geological Survey, P.O. Box 25046, MS 966, Denver, Colorado 80225, USA (ghayes@usgs.gov; wald@usgs.gov)

Katie Keranen

Western Earthquake Hazards Team, U.S. Geological Survey, 70 Johnson Hall, Seattle, Washington 98195, USA

Now at School of Geology and Geophysics, College of Earth and Energy, University of Oklahoma, 100 East Boyd Street, Suite 710, Norman, Oklahoma 73019, USA.

[1] Ongoing developments in earthquake source inversions incorporate nonplanar fault geometries as inputs to the inversion process, improving previous approaches that relied solely on planar fault surfaces. This evolution motivates advancing the existing framework for constraining fault geometry, particularly in subduction zones where plate boundary surfaces that host highly hazardous earthquakes are clearly nonplanar. Here, we improve upon the existing framework for the constraint of the seismic rupture plane of subduction interfaces by incorporating active seismic and seafloor sediment thickness data with existing independent data sets and inverting for the most probable nonplanar subduction geometry. Constraining the rupture interface a priori with independent geological and seismological information reduces the uncertainty in the derived earthquake source inversion parameters over models that rely on simpler assumptions, such as the moment tensor inferred fault plane. Examples are shown for a number of well-constrained global locations. We expand the coverage of previous analyses to a more uniform global data set and show that even in areas of sparse data this approach is able to accurately constrain the approximate subduction geometry, particularly when aided with the addition of data from local active seismic surveys. In addition, we show an example of the integration of many two-dimensional profiles into a three-dimensional surface for the Sunda subduction zone and introduce the development of a new global three-dimensional subduction interface model: Slab1.0.

Components: 8122 words, 8 figures, 1 table.

Keywords: subduction zone processes; seismicity and tectonics; earthquake source observations; earthquake dynamics; megathrust earthquakes; fault geometry.

Index Terms: 7240 Seismology: Subduction zones (1207, 1219, 1240); 7230 Seismology: Seismicity and tectonics (1207, 1217, 1240, 1242); 7215 Seismology: Earthquake source observations (1240).

Received 19 May 2009; **Revised** 13 July 2009; **Accepted** 31 July 2009; **Published** 25 September 2009.

Hayes, G. P., D. J. Wald, and K. Keranen (2009), Advancing techniques to constrain the geometry of the seismic rupture plane on subduction interfaces a priori: Higher-order functional fits, *Geochem. Geophys. Geosyst.*, *10*, Q09006, doi:10.1029/2009GC002633.

1. Introduction

[2] Knowledge of the geometry of the fault plane ruptured in any given earthquake is a vital component for most forms of earthquake source inversions. *Hayes and Wald* [2009] presented a new approach to constrain the geometry of shallow subduction interfaces in an automated and a priori sense by combining several independent earthquake catalogs, bathymetry, and fault databases, and explicitly accounting for depth uncertainties and inverting for a most likely planar fault in a given location. *Hayes and Wald* [2009] also showed that planar solutions to these data are adequate for modeling the seismogenic zone in the majority of cases; indeed, many (if not all) of the earthquake source inversions which would benefit from these results require planar surfaces as an input.

[3] However, in reality, subduction interfaces as a whole are not planar, particularly in their shallowest sections above the seismogenic zone where slabs enter trenches with often near-horizontal dips, and in deeper sections below the seismogenic zone where slabs bend over and sink via gravitational forces. Furthermore, new approaches to earthquake source inversions facilitate the incorporation of nonplanar fault surfaces [e.g., *Wald et al.*, 2008]. With these issues in mind, we attempt here to improve the geometry constraint methods presented by *Hayes and Wald* [2009] by inverting supplemented data sets for best fitting nonplanar surfaces to better match the true nature of subduction zone interfaces in all sections of the subduction zone from the trench to midmantle depths, while maintaining our focus on the shallow, seismogenic (and shallowest nonseismogenic) part of these plate boundaries.

2. Past Studies

[4] As discussed briefly by *Hayes and Wald* [2009], several previous studies have attempted to model Wadati–Benioff Zone (WBZ) geometry in subduction zones, particularly in the deeper parts of subduction below the seismogenic zone. Some of these concentrate on structure beneath volcanic arcs [e.g., *England et al.*, 2004; *Syracuse and Abers*, 2006], producing hand-drawn contours to match general WBZ structure, while others have produced more generalized multiregional [e.g., *Bevis and Isacks*, 1984] and global [e.g., *Gudmundsson and Sambridge*, 1998] models. Of these, the model of *Gudmundsson and Sambridge* [1998] is most comparable to our study, in that they produce three-dimensional surfaces of all global subduction zones by contouring EHB [*Engdahl et al.*, 1998] and International Seismological Center (ISC) catalog earthquake data. Slab contours are produced every 50 km in depth, and used in a Delaunay tessellation algorithm [e.g., *Okabe et al.*, 1992] to estimate slab volume in the mantle, which can be subsequently used to calculate the effects of slabs on earthquake travel times.

[5] We distinguish our model from these predecessors (1) by focusing mainly on the shallowest part of subducting slabs, where the greatest hazard from large megathrust earthquakes exists, while simultaneously attempting to honor the deeper structure of these slabs (this shallow focus is exemplified by attempting to resolve slab geometry on much finer scales than previous models); (2) by filtering the earthquake data sets used to include not only well-located (in depth) events, but also only those events with thrust mechanisms, thereby assuring we model only seismicity (and related structure) truly associated with the subduction process; and (3) by including additional data sets, such as subduction interface interpretations from high-accuracy active seismic profiles across trenches. In particular, this last step helps us to resolve slab geometry where seismicity rates are low or nonexistent, and thus facilitates a higher-resolution subduction geometry model.

3. Procedure to Constrain Slab Interface Geometry

[6] *Hayes and Wald* [2009] combine data from historic earthquake catalogs (global Centroid Moment Tensor (gCMT); National Earthquake Information Center Preliminary Determination of Epicenters (NEIC PDE)) and the global relocation catalog of *Engdahl et al.* [1998] (hereinafter referred to as EHB) and locations of trench breaks on the seafloor (from the plate boundary files of *Tarr et al.* [2009] and the Marine Geoscience Data System (MGDC) bathymetry database, http://www.marine-geo.org). A merged catalog is filtered to remove distant earthquakes (>100 km from a reference plane), events without well-constrained depths (following the analyses of *Engdahl et al.* [1998]) or CMT mechanisms (following the criteria of *Frohlich and Davis* [1999]), and events without thrust mechanisms ($45° < \lambda < 135°$, where λ is the rake angle of the nodal or auxiliary plane). Those events either in the upper plate or below the seismogenic zone are also removed. Uncertainties

Table 1. Locally Recorded Data Used to Aid Subduction Geometry Constraint[a]

Profile Location	Near Profile ID	References
Aleutians	fo2/kk1	*Holbrook et al.* [1999]
Fox Islands	fo3/kk2	*Ryan and Scholl* [1989]
Costa Rica	Nic	*Ye et al.* [1996], *Sallarès et al.* [1999], *Christeson et al.* [1999]
Nicaragua	ni2	*Walther et al.* [2000]
Peru	Per	*Krabbenhöft et al.* [2004]
S. Peru	pe2	*Hampel et al.* [2004]
N. Chile	Ant	*Patzwahl et al.* [1999]
N. Chile	ant	*Husen et al.* [1999]
N. Chile	ant/an4	*Sallarès and Ranero* [2005]
Chile	chi	*Krawczyk* [2006]
Solomon Islands	sol	*Fisher et al.* [2008]
Java	jav	*Kopp et al.* [2002]
S. Sumatra	in5/s10	*Kopp et al.* [2001]
N. Sumatra	su1/su4	*Franke et al.* [2008]
Marianas Islands	mar	*Oakley et al.* [2008]

[a] All local data are from active source surveys with the exception of *Husen et al.* [1999]. For each active source profile, we pick a sufficient number of well-distributed points to accurately reflect the geometry of the plate interface delineated by the data. The spacing and number of points chosen depend upon the geometry of each line and the resolution of the data used to image the plate interface.

in earthquake depths are incorporated to produce probability density functions for each location, through which a best fitting line is fit to represent the most likely planar subduction interface. We refer readers to *Hayes and Wald* [2009] for a more detailed discussion of their approach.

[7] As discussed by *Hayes and Wald* [2009], their planar interfaces may not match well the shallowest aseismic sections of slab interfaces near the trench, where earthquakes do not nucleate, but where slip may occur in large thrust events. In such cases, the incorporation of data from active seismic surveys across the trench would greatly improve the modeling of the subduction interface, and enable the inversion for nonplanar geometries that match both these shallow data and the earthquake locations within the seismogenic zone. These geometry inversions would also benefit from the inclusion of trench sediment thickness data, allowing us to model the true position of the plate interface at the trench rather than following the simplistic assumption that the most likely interface intersects the Earth's surface at the trench break on the seafloor. Where possible, we include such data in this study.

[8] *Hayes and Wald* [2009] also note that in some cases curvature of the subduction interface is evident before the base of the seismogenic zone. In these cases, the rollover of the slab cannot be reconciled with a planar interface, and a nonplanar surface may fit the data better, particularly if we extend our data set further to include deeper seismicity. While earthquakes below the seismogenic zone do not represent the subduction interface itself (rather, they are caused by internal deformation within the sinking slab), they can provide useful constraint on the approximate location of the slab and its geometry at depth.

[9] In this study, we adopt the same data sets and filters as *Hayes and Wald* [2009], with one small change to the approach used to constrain the strike of the reference profile: after computing the average strike of all CMTs from the merged catalog that pass initial filter criteria, we further filter the data set by removing outliers, defined as those events whose strike is greater than one standard deviation away from the mean strike angle. Having done so, the average strike is recomputed, and used to represent the regional subduction strike direction [*Hayes and Wald*, 2009]. In addition to these data, we include interpretations of shallow slab interfaces from active seismic data collected across trenches in a selection of locations (Table 1), local passive seismic deployments aimed and resolving detailed slab structure using high-accuracy hypocenters [e.g., *Husen et al.*, 1999], trench sediment thicknesses interpreted from the National Geophysical Data Center (NGDC) global sediment thickness map [*Divins*, 2009], and intermediate-depth seismicity (80–400 km) to aid in the constraint of the slab geometry below the seismogenic zone. For the profiles considered in this study (184 in total), the inclusion of trench sediment thickness data shifts the trench location to greater depths by an average 0.6 km. Intermediate depth seismicity is shifted a constant 10 km further from the trench to account for their occurrence below the plate boundary within the subducting plate (representing deformation internal to the slab) rather than on its interface (where seismogenic zone earthquakes are assumed to occur). This shift, while arbitrary, allows us to better fit the surface of the deeper slab rather than the center of the spread of hypocenters.

[10] We have tested fitting these data using a number of minimization approaches, including multiple-order LU decomposition and Minimum Norm solutions, and spline fits. In general we find that spline fits do the best job of matching all data at the same time as maintaining a surface that appears geophysically reasonable, i.e., smooth and without abundant inflection points to fit changes in data trends. Furthermore, our tests show

that spline fits do a much better job where data are lacking; in such instances, high-order polynomial fits add artifacts of excessive curvature that are both unwarranted and unreasonable. For these reasons, in this study we present nonplanar surfaces produced by Hermite Spline fits, interpolating between (1) minimum norm solution to shallow (<80 km) data only, polynomial of order 2–3, and (2) minimum norm solution to intermediate-depth data plus average of last 10% of shallow data points (i.e., those furthest from the trench), polynomial of order 3–4.

[11] We assess which spline solution fits all of the data best in a weighted least squares sense (see auxiliary material Text S1 (Table S1)), accounting for changes in the number of free parameters in the shallow and deep polynomial fits, and choose this as the corresponding solution at the reference location.[1] In a limited number of cases for which the resulting nonplanar fit appears geophysically unreasonable (inflection toward the surface of the Earth, or excessive rollover not apparent in data), control points are added on the basis of a visual estimate of the slab location. For any one profile, no more than two control points are added. Of 184 profiles considered here, just 14 required control points.

[12] These calculations result in the most probable nonplanar geometry of the subduction thrust interface near the reference location that is consistent with shallow and intermediate-depth seismicity data, active source seismic data across the trench (if available), and the location of the trench on the seafloor.

4. Data Integration and Weighting

[13] As we are combining different types of data, we must also assign each data set (and each individual point) a relative weighting that acts as a measure of uncertainty in that data location. Each earthquake location used has an associated uncertainty from the EHB catalog, or an assigned uncertainty based on a comparison of the PDE and EHB catalogs [*Hayes and Wald*, 2009] which we use as a measure of the uncertainty of the individual data point. When using local active seismic data, we adopt the uncertainties in depth reported by the authors, if available; otherwise the depths receive a standard weight of ±2 km. For most active seismic data used, this uncertainty is pessimistic and can be considered a worst-case scenario. When combining data sets, relative weighting is assigned as follows: local active seismic data are weighted ten times that of shallow (seismogenic zone) earthquake data, which are in turn weighted twice that of intermediate-depth earthquake data. These relative weights have been assigned both on the basis of the perceived importance of the data sets in constraining the form of the best fitting nonplanar surface and through a trial-and-error process of testing different relative weighting schemes.

5. Geometries of Global Subduction Zones

[14] As in *Hayes and Wald* [2009], we have applied our procedure in seismically active subduction zones worldwide. All of the locations in the original study are included, in addition to several new locations (Figure 1). Three examples are shown here – others can be found in Text S1. In section 5.2, we directly assess the benefit of using active seismic data as an additional geometry constraint by comparing profiles with and without these data included.

[15] Our first example shows results offshore of northern Sumatra, using the M_w 7.4 earthquake of 20 February 2008 as the reference location. In the same region, *Franke et al.* [2008] collected wide-angle/refraction seismic data and multichannel seismic data that image the subduction interface across the trench and which are used for additional constraint on the location of the plate boundary. When combined, these active source and earthquake data complement each other well and delineate a subduction interface that varies in dip from ~0° at the trench to ~20° 250 km inboard of the trench (Figure 2). Between ~160–240 km, the slab interface flattens slightly, indicated by both an inversion in the dip of the nonplanar interface, and by the trend in background seismicity. This feature is common to adjacent cross sections along strike in the Sunda subduction zone (Text S1). Further downdip, the slab continues to roll over and the best fitting nonplanar surface matches the locations of intermediate-depth earthquakes between the depths of 80–180 km at distances of 250–360 km from the trench. In this solution, the subduction direction is constrained by the strike of 90 gCMT solutions, while the dipping interface is best matched by a Hermite Spline interpolation between a third-order polynomial fit to the shallow

[1] Auxiliary materials are available in the HTML. doi:10.1029/2009GC002633.

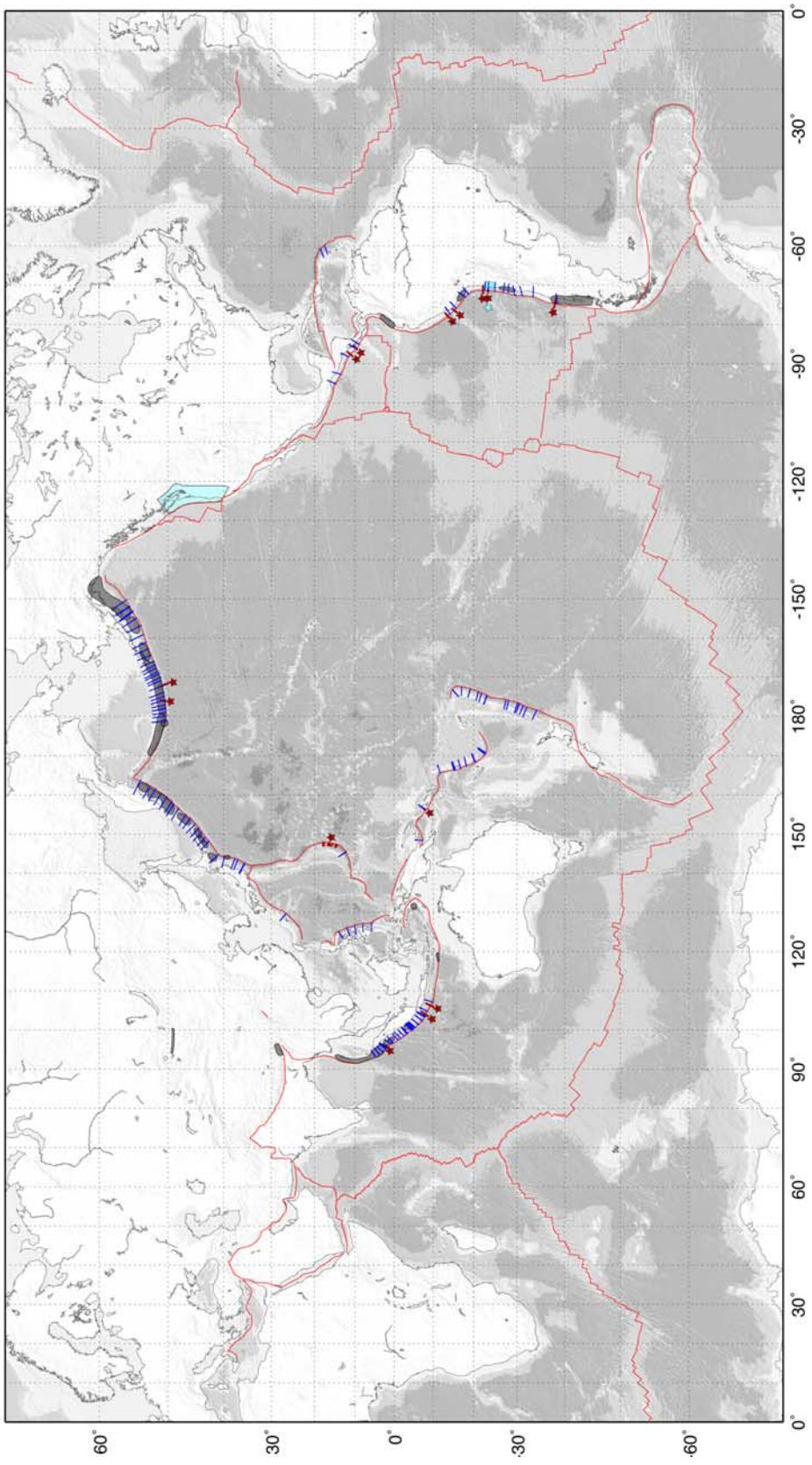

Figure 1. Global map of subduction zones studied in this analysis, overlain on global bathymetry from the Marine Geoscience Data System (MGDC) bathymetry database (http://www.marine-geo.org). Small blue lines denote locations where subduction geometry has been constrained in this study. Red lines indicate locations of data interpreted from local active seismic surveys listed in Table 1 (each line also denoted by red stars). Light blue shaded areas indicate regions of data available from local passive seismic deployments (each area also denoted by a blue star). Light blue shading in northwestern USA outlines the area constrained by the Cascadia subduction zone geometry model of *McCrory et al.* [2004]. Rupture zones of historic great earthquakes since 1900 are shaded gray [*Tarr et al.*, 2009]. Global plate boundaries are shown in red [from *Tarr et al.*, 2009].

earthquake and local active seismic data and a separate third-order polynomial fit to the intermediate-depth earthquake data. This solution uses 40 EHB locations, 5 PDE locations, and 35 data points interpreted from the active seismic data of *Franke et al.* [2008]. In addition, 7 intermediate-depth earthquakes are used to constrain the deeper form of the inferred interface.

[16] At the centroid location of the reference event, our inversion suggests an interface dip of 15°, compared to 11° for the corresponding fault plane of the gCMT solution. Figure 2d shows the variation in dip of the fault planes of CMT solutions used as constraints in the inversions versus distance along the cross section, and implies that CMT dips are on average higher than the dip of the subduction interface, similar to the bias first identified by *Hayes and Wald* [2009], though (on average) the bias suggested by the nonplanar interface is lower than that observed with respect

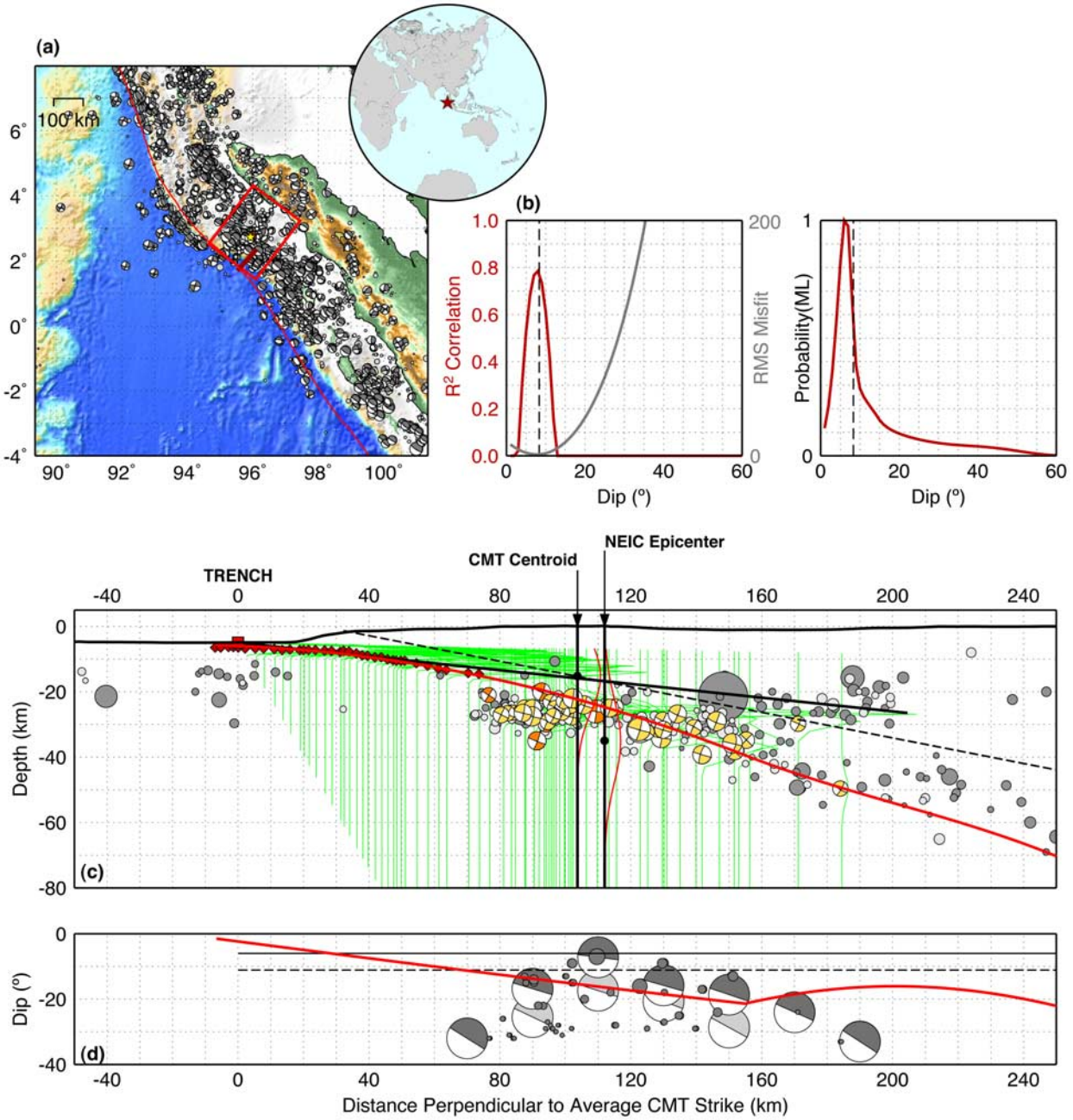

Figure 2

to planar interfaces. These issues are discussed further in section 5.3.

[17] An interesting observation of this example is that the December 2004 M_w 9.2 Sumatra earthquake projects significantly above our inferred subduction (megathrust) interface in this region (Figure 2). While some of this discrepancy may be accounted for by depth uncertainty, the difference in depths (~15 km) is greater than the reported uncertainty of the earthquake hypocenter (~±5 km). It is also possible that this discrepancy results from projecting hypocenters that lie on opposite sides of structural complexities, such as slab breaks or tears, onto one cross section; such features have been proposed in this area of the Sunda subduction zone [e.g., *Pesicek et al.*, 2008], though hypocenters to the north and south of the reference profile in this example (dark versus light gray in Figure 2) occupy the same space in the cross section. Whatever the cause of the misfit, it suggests that the depth of the hypocenter and dip of the plane used for earthquake source inversions for this event may contain more uncertainty than previously assumed, and accuracy may be improved by the consideration of deeper nucleation and a more inclined plane.

[18] Our second example is centered offshore northern Chile, at the location of the M_w 7.8 14 November 2007 earthquake (the same location as *Hayes and Wald* [2009, Figure 4]). In this region, *Patzwahl et al.* [1999] collected active seismic data across the trench, which we use for additional constraint. These data are best fit by a Hermine Spline interpolation between a third-order polynomial fit to the shallow earthquake and local active seismic data and a third-order polynomial fit to the intermediate-depth earthquake data. This spline increases in dip from close to 0°, 50 km outboard of the trench to ~25°, 250 km downdip of the trench axis (Figure 3). Here the dip decreases slightly to match a flattening in the trend of intermediate-depth earthquakes in this region, be-

Figure 2. Subduction interface geometry constraints for the Sunda Trench at the location of the 20 February 2008 M_w 7.4 earthquake. (a) Base map of Sunda subduction zone showing the area of the trench constrained in this example. Earthquake locations from the gCMT catalog (focal sphere mechanisms) and NEIC catalog (gray circles, sized according to magnitude) are shown. Red rectangle indicates the area shown in cross section (Figure 2c), extending 250 km downdip of the trench location; all earthquakes within this area may be used to constrain trench geometry. Red star indicates reference event (NEIC epicenter); yellow star represents the gCMT centroid location for reference event. Thick maroon lines crossing the trench highlight locations where data are available from local active seismic surveys. (b) Probability functions describing planar interface dip likelihood over a range of dips from 0°–60°. Results (right) from a maximum likelihood approach and (left) for weighted least squares (red and gray solid lines for correlation and misfit functions, respectively) and SVD (dashed black vertical line). (c) Cross section of subduction zone taken perpendicular to the average strike of gCMTs that match selection criteria and whose equivalent EHB or NEIC locations lie within the red box from Figure 2a. Gold CMTs are mechanisms from the gCMT catalog plotted at their equivalent EHB catalog location, used to constrain trench strike and dip. Orange CMTs are mechanisms without EHB locations, placed instead at the equivalent event location in the NEIC catalog, and also used to constrain geometry. Local active seismic data are identified by maroon diamonds, where available. Light and dark gray circles are events from the EHB catalog in front of and behind the plane of the cross section, respectively. Those not overlain with CMTs as described above are not used to constrain geometry because either (1) they did not have a corresponding mechanism in the gCMT catalog or (2) their mechanism in the gCMT catalog did not match selection criteria. The approximate location of the plate boundary at the trench is marked with a red square and labeled "Trench." Probability density functions for EHB and NEIC locations are shown as green lines, scaled by a factor of ×20 for display purposes. The black solid line describes the best fitting planar geometry. The red solid line describes the best fitting nonplanar geometry. The initial locations of the "new event" used to help constrain geometry are shown by black circles and marked with arrows corresponding to the gCMT epicentroid and NEIC epicenter. PDFs for these locations are shown in red. The best fitting fault plane from the gCMT catalog for the new event is shown with a black dashed line. (d) Variation in dip of best fitting fault planes from the gCMT catalog for all events used to constrain trench geometry across the plane of the cross section. Individual event dips are shown with small dark gray circles, sized with magnitude. Large mechanisms indicate the average dip in 20 km bins across the plane of the cross section. Light gray mechanisms represent a bulk average; dark gray represents a moment-weighted average. Black dashed line indicates the dip of the best fitting planar solution; red dashed line is for the nonplanar solution. (e) Extended cross section from Figure 2c, including intermediate-depth earthquakes (80–400 km) in maroon, used to help constrain the form of the nonplanar geometry. Results of bootstrapping uncertainty analysis for the nonplanar geometry constraint are shown in thin gray lines, behind the most likely interface (red). The blue dashed line represents a projection of the slab interface from the RUM model [*Gudmundsson and Sambridge*, 1998] into the plane of the cross section.

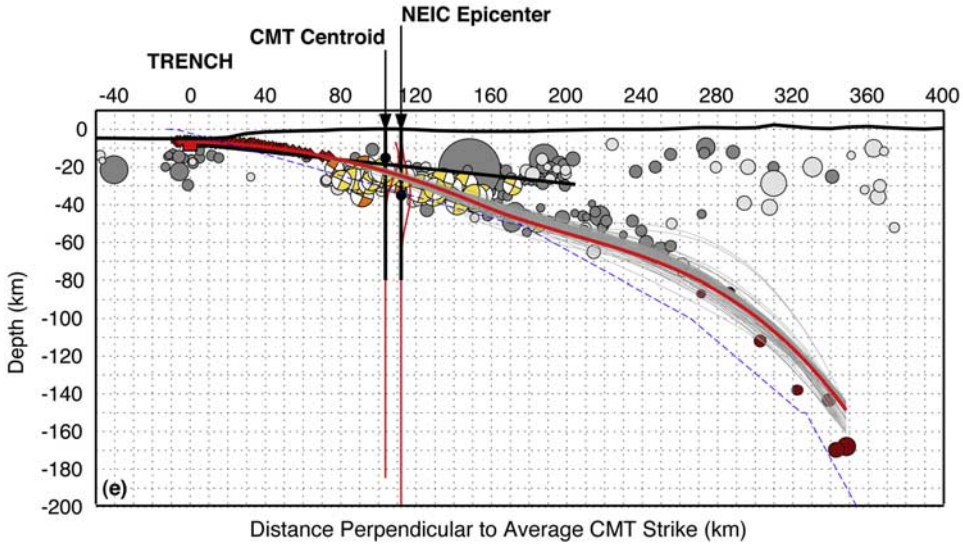

Figure 2. (continued)

fore increasing beyond ~400 km where the slab rolls over once more. In this solution, the subduction direction is constrained by 17 gCMT solutions, while the spline uses 3 EHB locations, 3 PDE locations, and 28 data points interpreted from the active seismic data of *Patzwahl et al.* [1999]. In addition, 500 intermediate-depth earthquakes are used to constrain the deeper form of the inferred interface. As these data suggest, the inversion for interface geometry in the shallow, seismogenic portion of the subduction zone at this location is dominated by the inclusion of data from local sources, illustrating the importance of obtaining such data in regions where background seismicity is sparse, scattered, or not related to subduction. It is encouraging that this solution also agrees well with the best fitting planar interface for the same location in the work of *Hayes and Wald* [2009], which had a dip of 11° versus a planar solution dip of 9° implied here. The corresponding fault plane of the gCMT solution for this event had a dip of 20°E. At this location, the nonplanar interface dips at 15°.

[19] In the same region of northern Chile, *Husen et al.* [1999] collected passive seismic data from a local array of seismometers deployed above the subduction zone in 1995 to record aftershocks of the nearby 30 July 1995 megathrust earthquake. We do not incorporate these data directly into our inversion because information on their faulting mechanisms is not known; however, we can use the locations of these recorded aftershocks to independently constrain the geometry of the local slab interface, without teleseismic data. We find that the distribution of the locally recorded aftershocks is very similar to that of larger, teleseismic events used for our global constraint approach, and geometry differences between solutions derived from the two data sets are <2° in dip and <5 km in depth over the range of the data (i.e., within the seismogenic zone).

[20] Our third example is located offshore central Honshu, Japan. Currently, we do not have access to local active seismic data in this area (though such data exists, and can be added at a later date). As such, the polynomial is constrained only by shallow and intermediate-depth earthquakes (Figure 4). In this case, the Hermine Spline interpolates between separate third-order polynomial fits to the shallow and intermediate-depth earthquake data, respectively. The dip of this surface increases from 0° at the trench to ~25° 250 km downdip. The subduction direction is constrained by 114 gCMT solutions, while the spline uses 76 EHB locations, 2 PDE locations, and 82 intermediate-depth earthquakes. Figure 4d shows that CMT dips are on average higher than the dip of the subduction interface, as in our first example, but again that this bias is somewhat reduced by the nonplanar interface geometry compared to the planar geometry considered in *Hayes and Wald* [2009].

5.1. Uncertainty Assessments

[21] In addition to the uncertainty estimates provided via a weighted least squares misfit comparison between data and nonplanar fits (Text S1 (Table S1)), we have performed bootstrap analyses

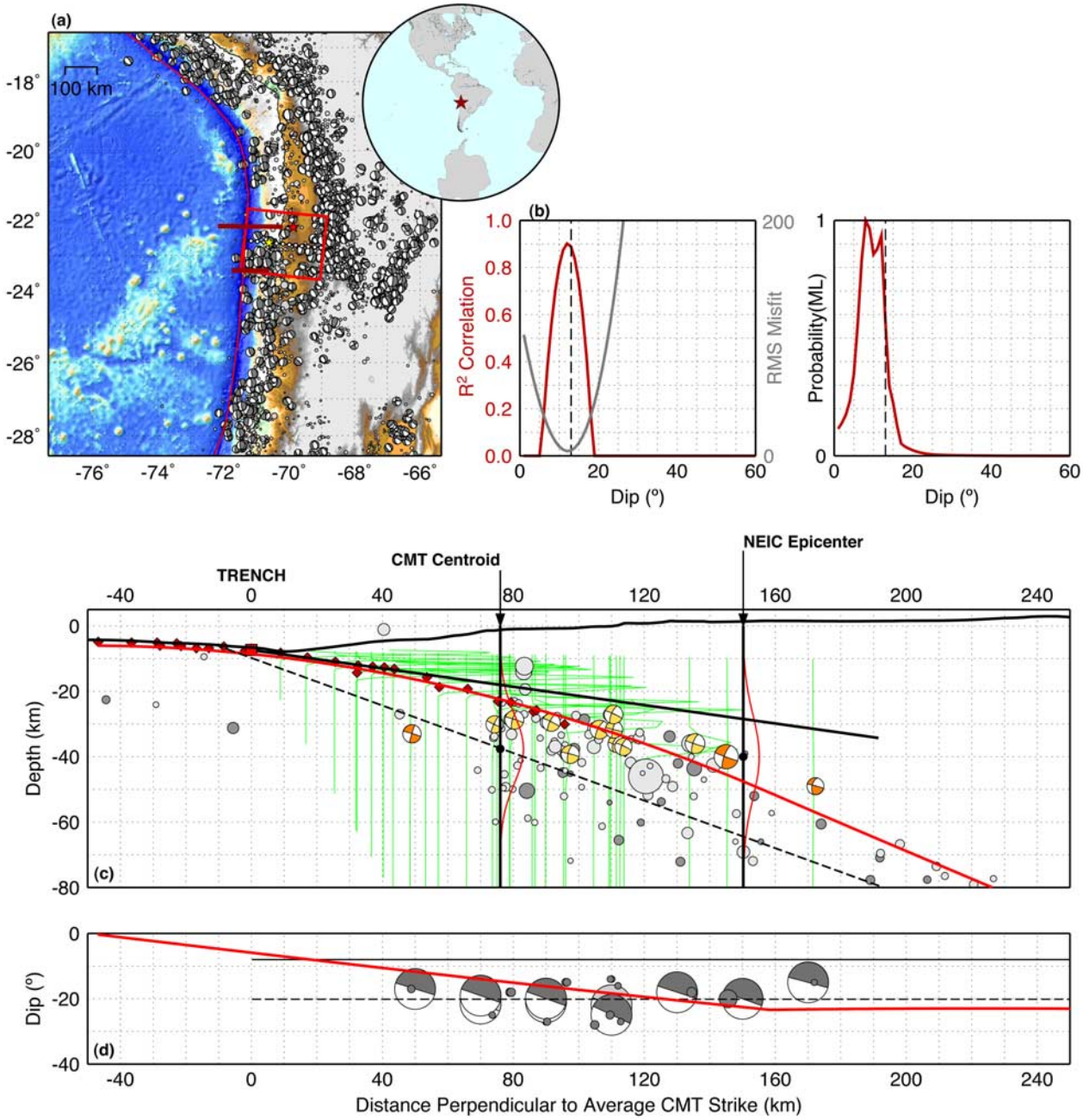

Figure 3. Subduction interface geometry constraints for the Northern Chile Trench at the location of the 14 November 2007 M_w 7.8 Antofagasta earthquake. See Figure 2 caption for descriptions of all symbols and labels. (a) Base map of Northern Chile subduction zone showing the area of the trench constrained in this example. (b) Probability function describing planar interface dip likelihood. (c) Cross section of subduction zone taken perpendicular to the average strike of gCMTs, used to constrain subduction zone interface dip. (d) Variation in dip of best fitting fault planes from the gCMT catalog for all events used to constrain trench geometry across the plane of the cross section. (e) Extended cross section from Figure 3c, including intermediate-depth earthquakes in maroon (80–400 km), used to help constrain the form of the nonplanar geometry. Results of bootstrapping uncertainty analysis are shown in thin gray lines, behind the most likely interface (red). The blue dashed line represents a projection of the slab interface from the RUM model [*Gudmundsson and Sambridge*, 1998] into the plane of the cross section.

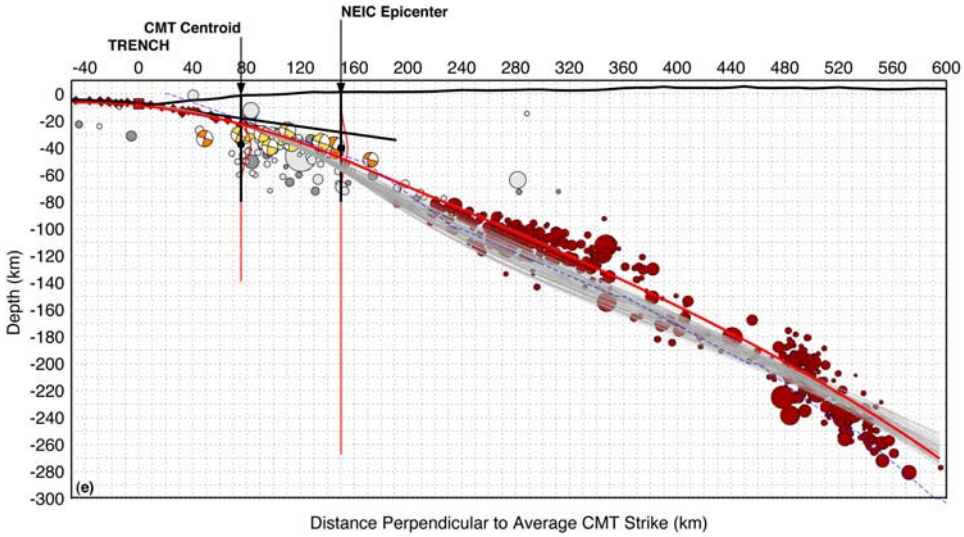

Figure 3. (continued)

[e.g., *Efron and Tibshirani*, 1993] for each profile location to estimate the potential variability in our solutions given a randomly adjusted data set. At a given location, a new data set is created via random selection with replacement of the original data set, such that any one data point may be used multiple times and the size of the resampled data set is the same as that of the original. We note that bootstrap analysis assumes data are independent and identically distributed. In this analysis, we use depths from the EHB and PDE catalogs, which are independently calculated (i.e., they do not rely on the depths of other events), and we assume Gaussian distributions for depth uncertainties. If the latter is not true for all data, the uncertainties resulting from this analysis may tend to be low. This resampling and assessment is repeated 100 times, and the resulting geometry estimates are plotted in gray on Figures 2e, 3e and 4e, and part (e) of each example included in Text S1. As this bootstrapping analysis is meant only to assess the potential scatter of our most likely interfaces and where each is well sampled by data, individual best fit surfaces derived from data subsets have not been constrained to be physically reasonable in the same manner as the most likely best fit surface for all data. Nevertheless they allow us to visually assess how well the data available to us constrains each interface.

5.2. Benefit of Active Seismic Data

[22] Here we assess the benefit of using additional active shallow seismic data to help constrain the form of the slab interface near the trench, by comparing inversions with and without these data in an area where the seismogenic zone and deeper slab are well populated with seismicity (i.e., where solutions without active data are still well constrained). Our example is centered offshore of southern Sumatra, near 7.5°S, 103°W (Figure 5). The profile strike is constrained by 30 gCMT solutions, and the nonplanar fit to the dipping subduction interface uses 12 EHB earthquake locations, 1 PDE location and 12 intermediate-depth earthquakes. When local active seismic data are incorporated, we use 17 data points interpreted from the active source profiles collected in the region by *Kopp et al.* [2001].

[23] Though the most likely nonplanar interfaces with and without additional local active seismic data are very similar (Figure 5), the bootstrapping analysis reveals much broader uncertainty in the shallow slab section for the solution without local active seismic data, due to a lack of earthquakes in the first ~150 km downdip of the trench. The addition of the local data significantly improves our resolution of this region, enabling a confident interpretation of the slab interface joining the trench to the earthquakes further downdip in the seismogenic zone. Significant differences are also noticeable in the planar fits to the two data sets. With all data (active plus shallow earthquakes), the most likely planar interface dips at an angle of 4°, versus an 11° dip for the planar fit using just the shallow earthquake data, reflecting changes in geometry of this slab interface with depth not captured by the earthquake data.

[24] In other locations, such as the northern Sumatra example in Figure 2, removing local active

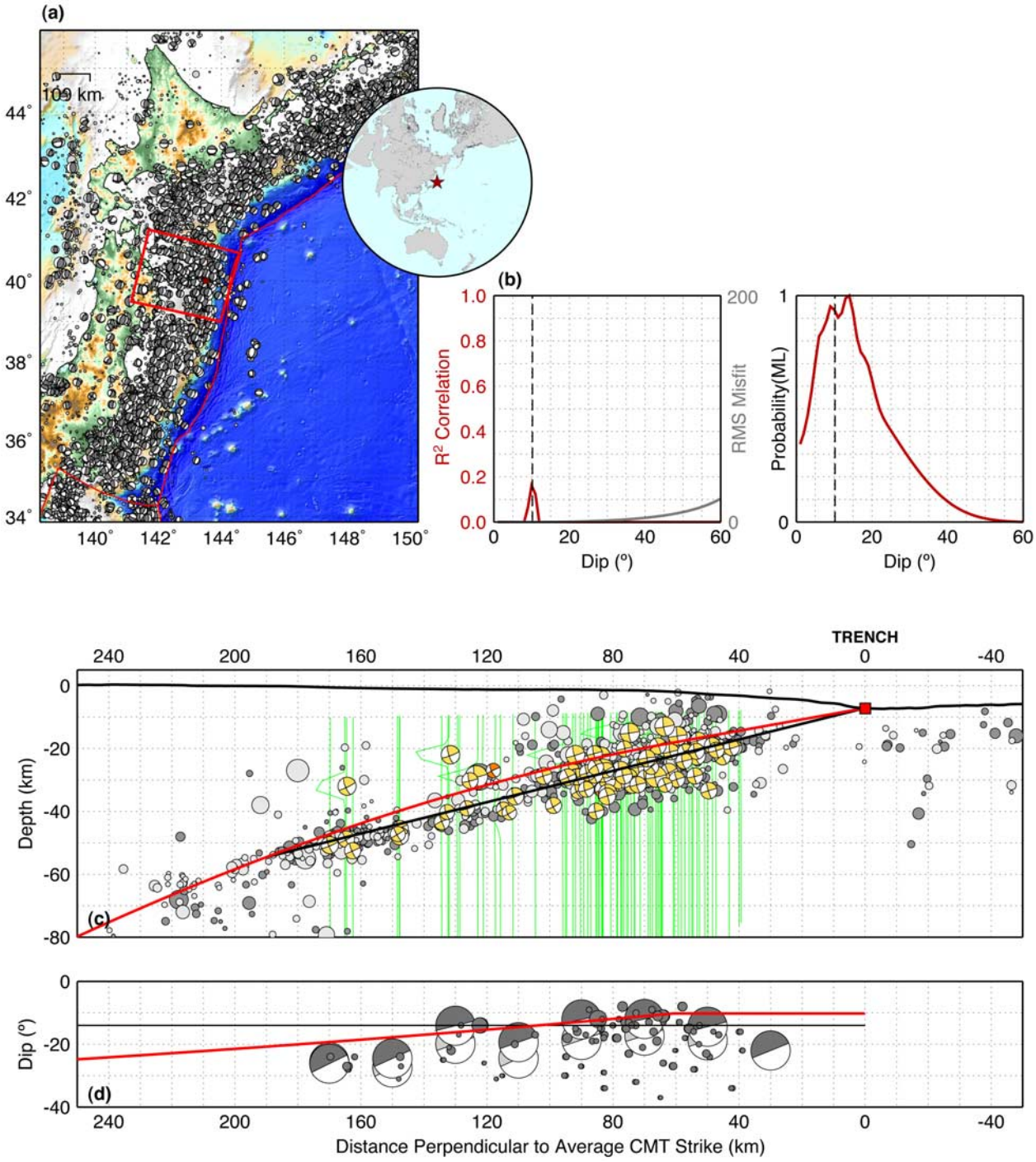

Figure 4. Subduction interface geometry constraints for the Japan Trench offshore northern Honshu. See Figure 2 caption for descriptions of all symbols and labels. (a) Base map of Japan Trench subduction zone showing the area of the trench constrained in this example. (b) Probability function describing planar interface dip likelihood. (c) Cross section of subduction zone taken perpendicular to the average strike of gCMTs, used to constrain subduction zone interface dip. (d) Variation in dip of best fitting fault planes from the gCMT catalog for all events used to constrain trench geometry across the plane of the cross section. (e) Extended cross section from Figure 4c, including intermediate-depth earthquakes (80–400 km) in maroon, used to help constrain the form of the nonplanar geometry. Results of bootstrapping uncertainty analysis are shown in thin gray lines, behind the most likely interface (red). The blue dashed line represents a projection of the slab interface from the RUM model [*Gudmundsson and Sambridge*, 1998] into the plane of the cross section.

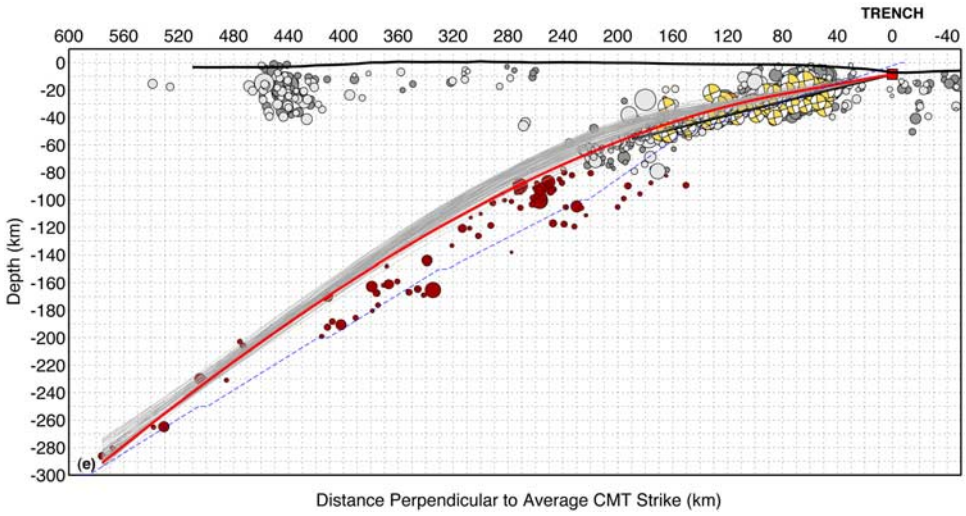

Figure 4. (continued)

seismic data causes the most likely nonplanar interface to favor a Hermite Spline interpolation between a second-order plane in the shallow section and a third-order polynomial at depth, rather than two third-order polynomials when shallow data are included. This switch tends to cause an overestimation of the depth of the subduction interface close to the trench, and reveals the importance of shallow data in areas of otherwise low data coverage. We show a comparison between nonplanar fits with and without local active seismic data in Text S2, for each location where such data are available (Table 1).

[25] As different data sets are used to constrain solutions with and without local active seismic data, and thus individual data weighting and relative weights are slightly different, it is difficult to quantitatively compare the two. However, if we compute an RMS misfit between the data points used for the solution with all data, and the most likely interface computed without the local active seismic data, we can approximately assess how much the local data improves our solution in this example. Such a comparison shows that adding the local active seismic data reduces the RMS misfit by ~21%. On average, for those locations where active source data are available, including these data reduces RMS misfits for nonplanar fits by ~22%.

[26] These comparisons highlight the importance of active source data for aiding the constraint of the shallowest part of the subduction interface, where earthquakes do not nucleate. Though in some cases the differences in nonlinear fits with and without such data are less significant (e.g., in5 in Figure 5 versus su4 in Figure 2 and Text S2, p. 9), when the shallow interface has a low angle of dip best fits between the trench and earthquake data further downdip are likely to overestimate the dip of the upper aseismic section of the slab. These data become particularly important if planar solutions are used, as in many cases there can be a significant difference between the trend of shallow active seismic data and deeper seismogenic zone earthquake data that cannot be captured in a linear data fit.

5.3. Dip Discrepancy?

[27] *Hayes and Wald* [2009] observed a difference between the dips of their inverted planar slab interfaces and the dips of the best fitting fault planes of gCMT mechanisms for events occurring

Figure 5. Subduction interface geometry constraints for the southern Sumatra Trench near the active source profiles of *Kopp et al.* [2001], comparing solutions with and without the inclusion of interface depths inferred from active source studies (local data). See Figure 2 caption for complete descriptions of all symbols and labels. (a) Base map of southern Sumatra subduction zone showing the area of the trench constrained in this example. Red rectangle indicates the area shown in cross sections in Figures 5b and 5c. All earthquakes within this area may be used to constrain trench geometry. (b) Geometry constraint using teleseismic and local active seismic data. Cross section of subduction zone taken perpendicular to the average strike of gCMTs, used to constrain subduction zone interface dip. (c) Geometry constraint using teleseismic data only; otherwise as Figure 5b.

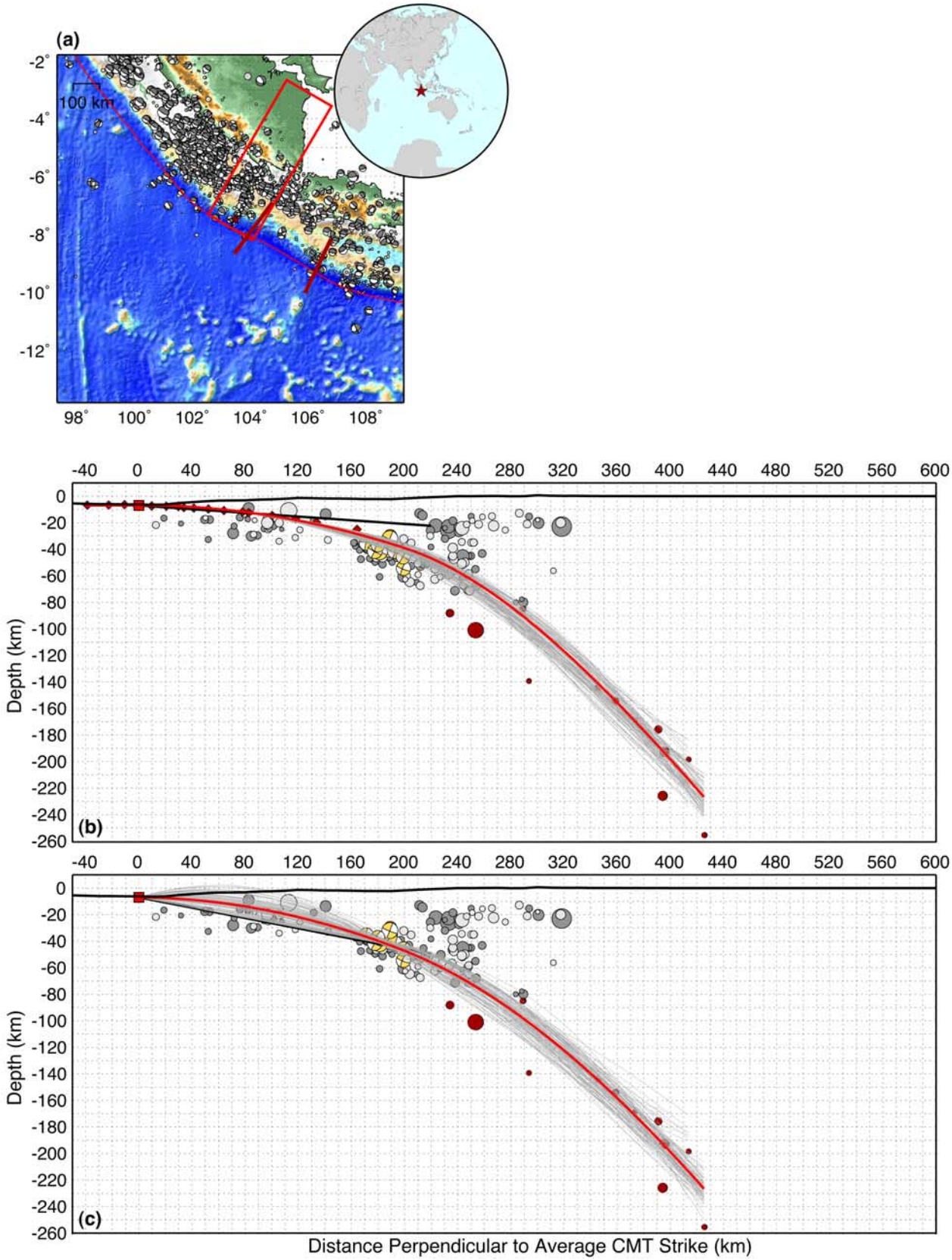
(a)
100 km
-2°
-4°
-6°
-8°
-10°
-12°
98°
100°
102°
104°
106°
108°
-40 0 40 80 120 160 200 240 280 320 360 400 440 480 520 560 600
0 -20 -40 -60 -80 -100 -120 -140 -160 -180 -200 -220 -240 -260
Depth (km)
(b)
(c)
Distance Perpendicular to Average CMT Strike (km)

Figure 5

on or close to those interfaces, biased on average ~9° toward oversteepened gCMT dips, and consistent for all subduction zones analyzed. Here, we have both reanalyzed the earlier comparison of gCMT dips with best fitting planar interfaces using our updated data sets and slightly revised inversion approaches, and in addition have performed the same comparison using our new nonplanar interfaces at each subduction zone. In the latter case, we compare the dips of the gCMT mechanisms with the dip of the best fitting nonplanar interface at the same distance from the trench axis.

[28] Figures 6 (planar solutions) and 7 (nonplanar solutions) show the results of this comparison. Figure 6a suggests a slightly greater bias (~12°) between gCMT dips and planar interfaces than that described by *Hayes and Wald* [2009]. Figure 7a shows that although this bias is reduced when gCMT dips are compared to nonplanar interfaces (~7–11°), a significant difference remains that does not appear to be related to our inversion approach. Furthermore, Figure 7d shows that the dependency of this bias on magnitude also remains for nonplanar interface comparisons, adding credence to the proposal by *Hayes and Wald* [2009] that the discrepancy may be a real signal associated with fault zone structure in subduction zones. Further investigation is required to fully resolve what component of this signal is related to uncertainties in CMT inversion procedures (if any). Verification of the origins of this discrepancy may help us address fundamental questions of how moment is released on subduction zone megathrusts during earthquake cycles.

6. Discussion and Conclusion

[29] This work extends the subduction interface geometry constraint method first presented by *Hayes and Wald* [2009] to include shallow active source data, other local data sets such as those of high-precision microearthquake locations, estimates of sediment thickness, intermediate-depth earthquakes, and the subsequent simultaneous inversion of all data to produce a best fitting nonplanar solution for the slab surface. This approach allows us to better fit the true curved form of subduction interfaces, rather than approximating the shallow seismogenic zone with planar geometries. A statistical comparison of RMS misfits between all data used to construct each nonplanar solution and respective best fitting planar and nonplanar solutions (over the X range for which planar solutions are valid) for 184 locations worldwide shows that, on average, nonplanar solutions offer a 14% improvement over planar fits. We also show that the inclusion of local active source data in nonplanar fits offers an approximate 22% improvement over similar solutions without local data, suggesting that the best way forward for subduction zone geometry modeling involves the systematic integration of seismic catalogs and local active seismic data wherever possible.

[30] The inclusion of local active seismic data also shows clear advantages in areas where background seismicity is diffuse (e.g., Cascadia, Southern Chile), or where interface seismicity is difficult to distinguish from upper plate seismicity (e.g., Solomon Islands). These locations were identified as areas where the planar geometry fits break down in the work of *Hayes and Wald* [2009]; here we show that the subduction interface can be more clearly resolved with the integration of more data (e.g., Text S2, pp. 3 and 22).

[31] The applicability of the automated approach to constrain nonplanar subduction geometry presented in this study over a broad range of subduction regimes (Text S1) speaks to the stability of our geometry inversion techniques. As we integrate more and more local and regional data with the preexisting catalogs of historic teleseismic data already in use, we will gain the ability to constrain the geometry of subducting slabs almost everywhere on the planet where at least some data exists. Such a step will facilitate moving from the 2-D approach we currently use to a fully three-dimensional model of subduction interfaces.

[32] The production of a three dimensional surface for any one subduction zone may reveal structure that helps to explain currently enigmatic patterns in subduction zone seismogenesis, such as the existence of structurally controlled segment boundaries, why certain ruptures terminate where they do, and quantitatively how big earthquakes can be in a given location. Figure 8 shows what a three-dimensional subduction interface derived from our methods may look like, using the Sunda subduction zone offshore of Sumatra as an example. Here, the high levels of seismicity, the existence of local active source data, and the relatively simple structure of the subduction zone with depth allow us to model the form of the interface accurately with a dense selection of cross sections along-strike, which we combine into a 3-D surface using the Generic Mapping Tools *grdsurface* algorithm [*Wessel and Smith*, 1991].

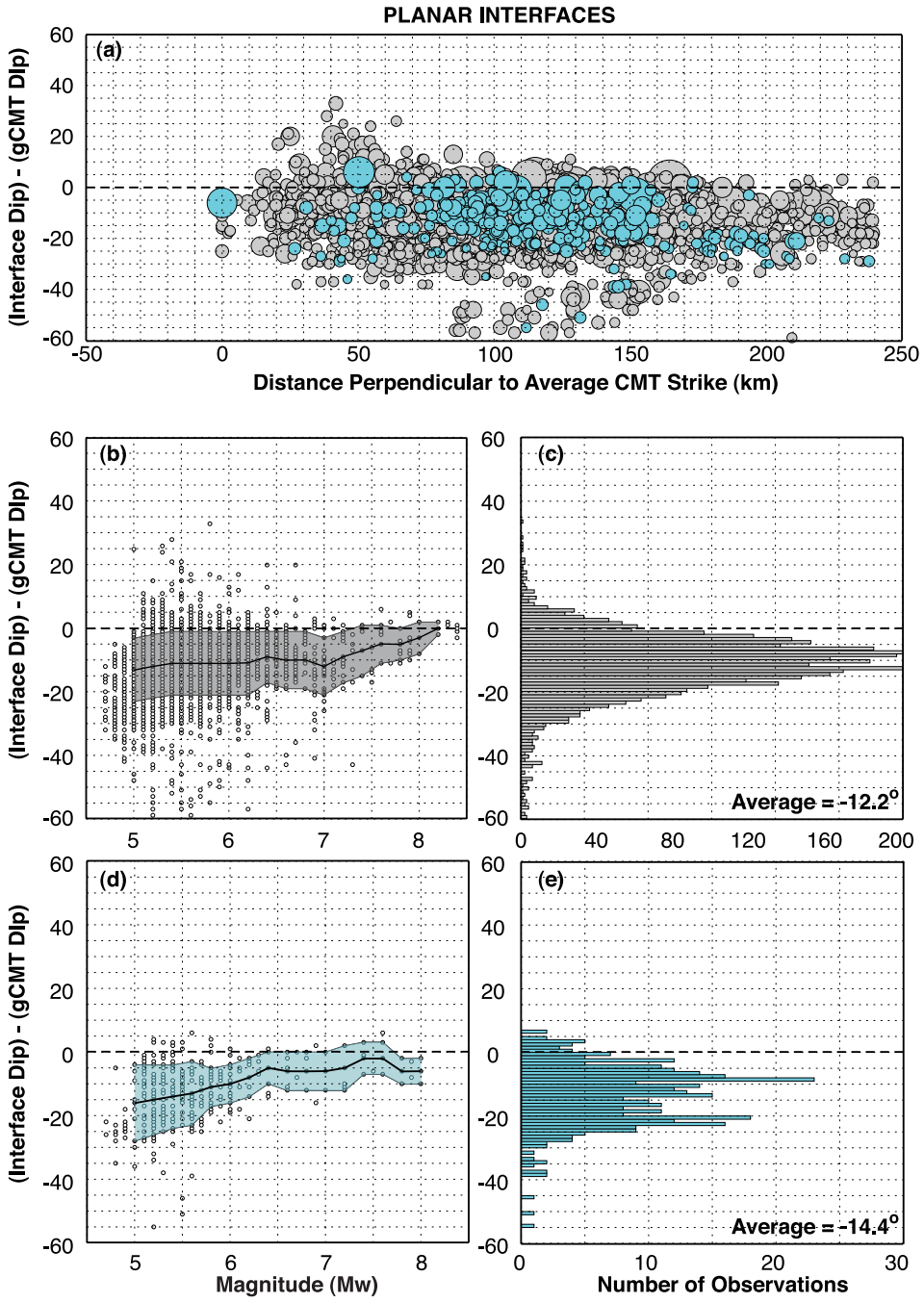

Figure 6. Comparisons of the difference in dip between our inverted planar interfaces and the individual mechanisms of moment tensor solutions for earthquakes along (and/or close to) those interfaces for all studied subduction zones globally. These results imply a bias toward steeper gCMT solution dips than inferred by our planar geometry inversions. (a) Dip discrepancy plotted as a function of distance from the trench. Gray circles are all observations; light blue circles correspond to solutions that include interface depths inferred using local active seismic data in their constraint. (b) We show this discrepancy as a function of magnitude for all solutions. White circles show individual observations; the dark line represents the average discrepancy for (M_w ± 0.5 magnitude units) in increments of 0.1 units, and the gray shaded region describes one standard deviation from that mean, suggesting a gradual trend for the highest-magnitude earthquake mechanisms ($\sim M_w > 7$) to be aligned more closely with the inferred subduction interface dip. (c) Histogram of results for all solutions in 1° bins. (d and e) We show the same plots as Figures 6b and 6c for those solutions that include local active seismic data (blue circles in Figure 6a).

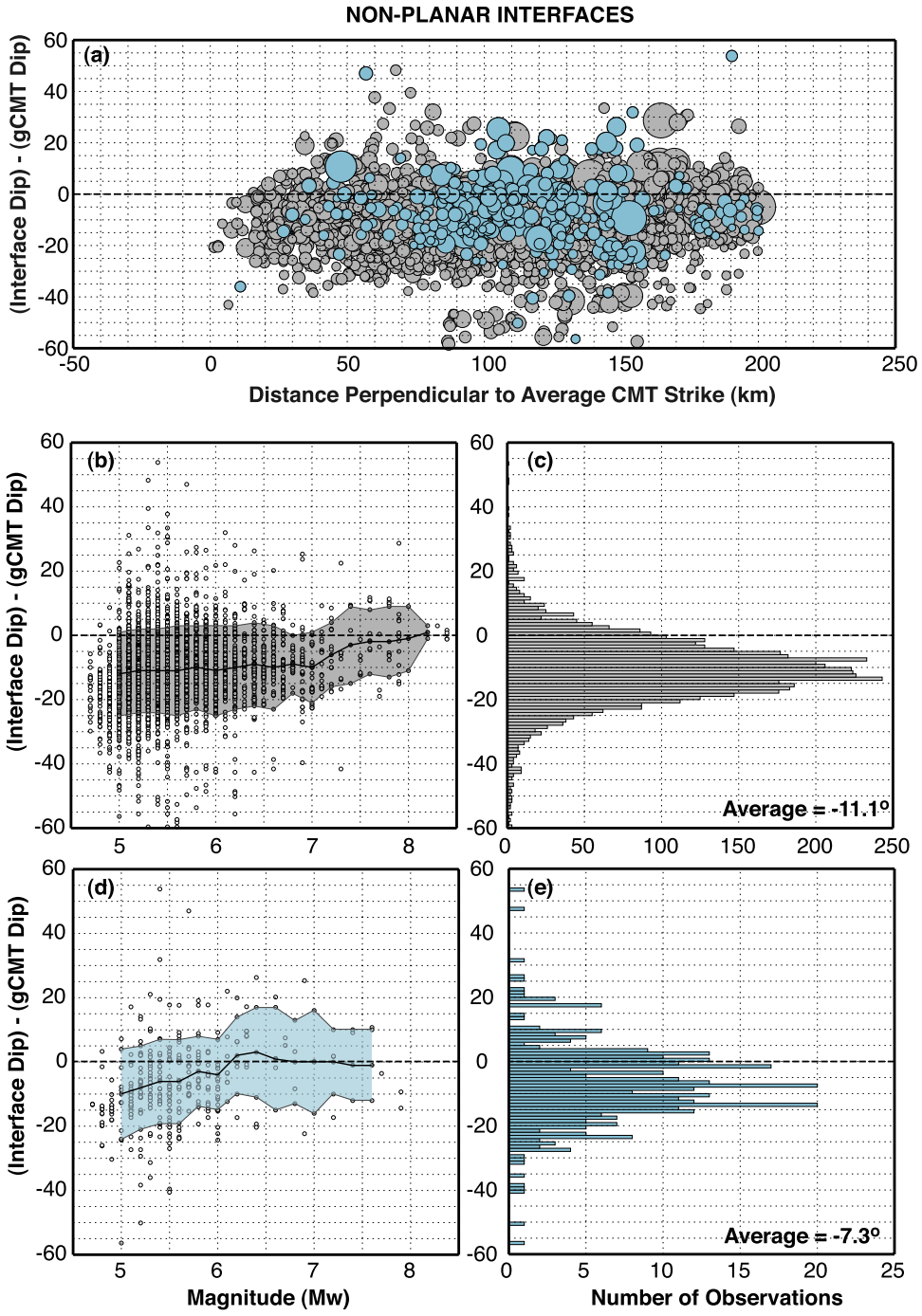

Figure 7. Comparisons of the difference in dip between our inverted nonplanar interfaces and the individual mechanisms of moment tensor solutions for earthquakes along (and/or close to) those interfaces for all studied subduction zones globally. For a description of each plot, see Figure 6 caption.

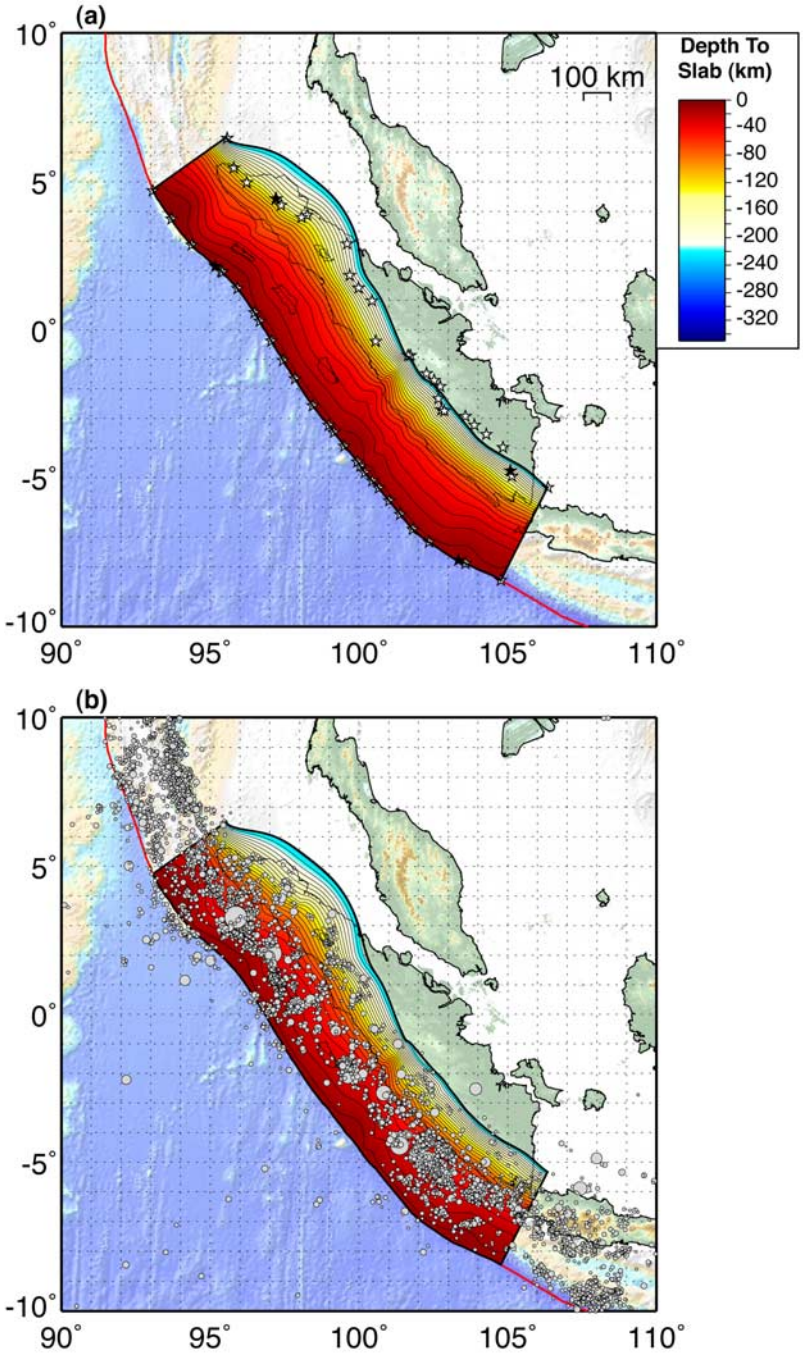

Figure 8. Three-dimensional surface for the Sunda subduction zone, built via interpolation between 18 individual two-dimensional profiles along the strike of the subduction zone. (a) Shown is this 3-D surface, colored by depth-to-interface. White stars indicate the ends of the 2-D profiles used. Black stars at ~1°N and ~8°S indicate profiles shown in Figures 2 and 5, respectively. (b) Shown is the same surface, overlain with seismicity from the EHB catalog.

[33] The construction of a global three-dimensional model, called Slab1.0, is currently underway, and will involve the interpolation of dense systems of 2-D cross sections along the strike of subduction zones into 3-D surfaces of their undulating interfaces. Future iterations will analyze various approaches of interpolating data to and representing data in three dimensions, how to incorporate segment boundaries into the model, and how best to represent data uncertainty in a globally consistent manner. Though derived primarily for a priori constraints for earthquake source inversions of future major subduction interface events, we envision broader applications for Slab1.0, including use

in seismic hazard calculations, tsunami modeling and response, 3-D wave propagation studies, and geodynamic modeling. This approach will allow us to not only capture the form of subduction plate boundary in the downdip direction, but along strike as well, creating the first global model of its kind.

Acknowledgments

[34] We thank Malcolm Sambridge and one anonymous reviewer for their helpful comments. We also thank Richard Briggs, James Dewey, Stephen Kirby, and the USGS Tsunami Source Working Group for comments and discussions during the preparation of this manuscript. Figures 1–8 were made using GMT, and we thank their developers and the users of their support list. Finally, we thank Bob Engdahl and the Global Centroid Moment Tensor Group for the maintenance of and open access to their respective earthquake catalogs. Gavin P. Hayes is contracted to work for the USGS by Synergetics, Inc., Fort Collins, CO.

References

Bevis, M., and B. L. Isacks (1984), Hypocentral trend surface analysis: Probing the geometry of Benioff zones, *J. Geophys. Res.*, *89*, 6153–6170, doi:10.1029/JB089iB07p06153.

Christeson, G. L., K. D. McIntosh, T. H. Shipley, E. R. Flueh, and H. Goedde (1999), Structure of the Costa Rica convergent margin, offshore Nicoya Peninsula, *J. Geophys. Res.*, *104*, 25,443–25,468, doi:10.1029/1999JB900251.

Divins, D. L. (2009), NGDC Total Sediment Thickness of the World's Oceans & Marginal Seas, http://www.ngdc.noaa.gov/mgg/sedthick/sedthick.html, World Data Cent. for Geophys. and Mar. Geol., Boulder, Colo.

Efron, B., and R. J. Tibshirani (1993), *An Introduction to the Bootstrap*, Chapman and Hall, New York.

Engdahl, E. R., R. D. Van Der Hilst, and R. P. Buland (1998), Global teleseismic earthquake relocation with improved travel times and procedures for depth determination, *Bull. Seismol. Soc. Am.*, *88*, 722–743.

England, P., R. Engdahl, and W. Thatcher (2004), Systematic variation in the depths of slabs beneath arc volcanoes, *Geophys. J. Int.*, *156*, 377–408, doi:10.1111/j.1365-246X.2003.02132.x.

Fisher, M. A., C. Ji, D. W. Scholl, F. L. Wong, and R. W. Sliter (2008), A revised slip model for the 2007 megathrust earthquake (M_w 8.1) in the Solomon Islands, *Seismol. Res. Lett.*, *79*, 354.

Franke, D., M. Schnabel, S. Ladage, D. R. Tappin, S. Neben, Y. S. Djajadihardja, C. Muller, H. Kopp, and C. Gaedicke (2008), The great Sumatra-Andaman earthquakes—Imaging the boundary between the ruptures of the great 2004 and 2005 earthquakes, *Earth Planet. Sci. Lett.*, *269*, 118–130, doi:10.1016/j.epsl.2008.01.047.

Frohlich, C., and S. D. Davis (1999), How well constrained are well-constrained *T*, *B*, and *P* axes in moment tensor catalogs?, *J. Geophys. Res.*, *104*, 4901–4910, doi:10.1029/1998JB900071.

Gudmundsson, O., and M. Sambridge (1998), A regionalized upper mantle (RUM) seismic model, *J. Geophys. Res.*, *103*, 7121–7136, doi:10.1029/97JB02488.

Hampel, A., N. Kukowski, J. Bialas, and C. Hübscher (2004), Ridge subduction at an erosive margin: The collision zone of the Nazca Ridge in southern Peru, *J. Geophys. Res.*, *109*, B02101, doi:10.1029/2003JB002593.

Hayes, G. P., and D. J. Wald (2009), Developing framework to constrain the geometry of the seismic rupture plane on subduction interfaces *a priori*—A probabilistic approach, *Geophys. J. Int.*, *176*, 951–964, doi:10.1111/j.1365-246X.2008.04035.x.

Holbrook, W. S., D. Lizarralde, S. McGreary, S. Bangs, and J. Diebold (1999), Structure and composition of the Aleutian island arc and implications for continental crustal growth, *Geology*, *27*, 31–34, doi:10.1130/0091-7613(1999)027<0031:SACOTA>2.3.CO;2.

Husen, S., E. Kissling, E. Flueh, and G. Asch (1999), Accurate hypocenter determination in the seismogenic zone of the subducting Nazca Plate in northern Chile using a combined on-/offshore network, *Geophys. J. Int.*, *138*, 687–701, doi:10.1046/j.1365-246x.1999.00893.x.

Kopp, H., E. R. Flueh, D. Klaeshen, J. Bialas, and C. Reichert (2001), Crustal structure of the central Sunda margin at the onset of oblique subduction, *Geophys. J. Int.*, *147*, 449–474, doi:10.1046/j.0956-540x.2001.01547.x.

Kopp, H., D. Klaeschen, E. R. Flueh, J. Bialas, and C. Reichert (2002), Crustal structure of the Java margin from seismic wide-angle and multichannel reflection data, *J. Geophys. Res.*, *107*(B2), 2034, doi:10.1029/2000JB000095.

Krabbenhöft, A., J. Bialas, H. Kopp, N. Kukowski, and C. Hübscher (2004), Crustal structure of the Peruvian continental margin from wide-angle seismic studies, *Geophys. J. Int.*, *159*, 749–764, doi:10.1111/j.1365-246X.2004.02425.x.

Krawczyk, C. M. (2006), Geophysical signatures and active teconics at the south-central Chilean margin, in *The Andes: Active Subduction Orogeny*, *Frontiers Earth Sci.*, vol. 1, edited by O. Oncken et al., pp. 171–192, Springer Verlag, Berlin.

McCrory, P. A., J. L. Blair, D. H. Oppenheimer, and S. R. Walter (2004), Depth to the Juan de Fuca Slab Beneath the Cascadia Subduction Margin—A 3-D model for sorting earthquakes, *U.S. Geol. Surv. Data Ser.*, *91*.

Oakley, A. J., B. Taylor, and G. F. Moore (2008), Pacific Plate subduction beneath the central Mariana and Izu-Bonin fore arcs: New insights from an old margin, *Geochem. Geophys. Geosyst.*, *9*, Q06003, doi:10.1029/2007GC001820.

Okabe, A., B. Boots, and K. Sugihara (1992), *Spatial-Tessellation Concepts and Applications of Voronoi Diagrams*, John Wiley, New York.

Patzwahl, R., J. Mechie, A. Schulze, and P. Giese (1999), Two-dimensional velocity models of the Nazca plate subduction zone between 19.5°S and 25°S from wide-angle seismic measurements during the CINCA95 project, *J. Geophys. Res.*, *104*, 7293–7317, doi:10.1029/1999JB900008.

Pesicek, J. D., C. H. Thurber, S. Widiyantoro, E. R. Engdahl, and H. R. DeShon (2008), Complex slab subduction beneath northern Sumatra, *Geophys. Res. Lett.*, *35*, L20303, doi:10.1029/2008GL035262.

Ryan, H. F., and D. W. Scholl (1989), The evolution of forearc structures along an oblique convergent margin, central Aleutian arc, *Tectonics*, *8*, 497–516, doi:10.1029/TC008i003p00497.

Sallarès, V., and C. R. Ranero (2005), Structure and tectonics of the erosional convergent margin off Antofagasta, north Chile (23°30′S), *J. Geophys. Res.*, *110*, B06101, doi:10.1029/2004JB003418.

Sallarès, V., J. J. Dañobeitia, E. R. Flueh, and G. Leandro (1999), Seismic velocity structure across the middle American landbridge in northern Costa Rica, *J. Geodyn.*, *27*, 327–344, doi:10.1016/S0264-3707(98)00007-6.

Syracuse, E. M., and G. A. Abers (2006), Global compilation of variations in slab depth beneath arc volcanoes and implications, *Geochem. Geophys. Geosyst.*, *7*, Q05017, doi:10.1029/2005GC001045.

Tarr, A. C., A. Villaseñor, H. M. Benz, and K. P. Furlong (2009), Seismicity of the Earth 1900–2007, *U.S. Geol. Surv. Sci. Invest. Ser.*, in press.

Wald, D., C. Ji, and G. P. Hayes (2008), Global earthquake characterization on irregular fault surfaces, *Eos Trans. AGU*, *89*(53), Fall Meet. Suppl., Abstract S31C-01.

Walther, C. H. E., E. R. Flueh, C. R. Ranero, R. von Huene, and W. Strauch (2000), Crustal structure across the Pacific margin of Nicaragua: Evidence for ophiolitic basement and a shallow mantle sliver, *Geophys. J. Int.*, *141*, 759–777, doi:10.1046/j.1365-246x.2000.00134.x.

Wessel, P., and W. H. F. Smith (1991), Free software helps map and display data, *Eos Trans. AGU*, *72*, 441, doi:10.1029/90EO00319.

Ye, S., J. Bialas, E. R. Flueh, A. Stavenhagen, and R. von Huene (1996), Crustal structure of the middle American trench off Costa Rica from wide angle seismic data, *Tectonics*, *15*, 1006–1021, doi:10.1029/96TC00827.